Parallel implicit contact algorithm for soft particle systems

Saeid Nezamabadi, Xavier Frank, Jean-Yves Delenne, Julien Averseng, Farhang Radjai

Parallel implicit contact algorithm for soft particle systems

Saeid Nezamabadi [a,*], Xavier Frank [b], Jean-Yves Delenne [b], Julien Averseng [a], Farhang Radjai [a,c]

[a] LMGC, Université de Montpellier, CNRS, Montpellier, France
[b] IATE, CIRAD, INRA, Montpellier SupAgro, Université de Montpellier, F-34060, Montpellier, France
[c] <MSE>^{2}, UMI 3466 CNRS-MIT, CEE, Massachusetts Institute of Technology, 77 Massachusetts Avenue, Cambridge 02139, USA

A B S T R A C T

This paper presents a numerical technique to model soft particle materials in which the particles can undergo large deformations. It combines an implicit finite strain formalism of the Material Point Method and the Contact Dynamics method. In this framework, the large deformations of individual particles as well as their collective interactions are treated consistently. In order to reduce the computational cost, this method is parallelised using the Message Passing Interface (MPI) strategy. Using this approach, we investigate the uniaxial compaction of 2D packings composed of particles governed by a Neo-Hookean material behaviour. We consider compressibility rates ranging from fully compressible to incompressible particles. The packing deformation mechanism is a combination of both particle rearrangements and large deformations, and leads to high packing fractions beyond the jamming state. We show that the packing strength declines when the particle compressibility decreases, and the packing can deform considerably. We also discuss the evolution of the connectivity of the particles and particle deformation distributions in the packing.

Keywords:
Material point method
Contact dynamics
Granular materials
MPI
Hyperelasticity
Finite strain

1. Introduction

The macroscopic behaviour of particulate materials is controlled by the microscopic mechanisms in terms of the interactions between individual particles as well as interactions with a surrounding fluid or confining walls. Understanding these mechanisms can be effectively achieved via particle scale simulation techniques based on microdynamic information. The Discrete Element Method (DEM) [1,2] and Contact Dynamics (CD) method [3–5] are recognised as efficient research tools for the investigation of the micromechanics of particulate materials. These methods are capable of dealing with different loading conditions, particle size distributions and physical properties of the particles. Such discrete simulations can provide detailed local information such as the trajectories of individual particles and transient forces acting on them that can be difficult to obtain by physical experimentation.

In the context of DEM methods, the particles are assumed to be hard or weakly deformable through different contact theories such as the Hertz contact theory, which is only valid up to about 10% of strain. However, this assumption is too crude in the application to highly soft particles such as metallic powders, many pharmaceutical and food products, and colloidal suspensions [6–10]. Soft particles may undergo large deformations without rupture. Hence, as the classical DEM techniques are intrinsically unable to account for realistic constitutive models for individual particles and large particle deformations, soft particle materials require a methodology capable of treating the contact interactions between particles as well as individual particle deformations.

We previously proposed a numerical procedure based on an implicit material point method (MPM) coupled with the CD method [11,12]. In the MPM, each particle is discretised by a set of material points carrying all state variables such as stress and velocity field. The MPM algorithm also uses a background grid for solving the momentum equations. The material points are assigned fixed masses during computation so that the conservation of mass is satisfied implicitly. The momentum changes are interpolated from the grid to the material points so that the total momentum is conserved. The implicit formulation allows for efficient coupling with implicit modelling of unilateral contacts and friction between the particles as in the CD method [3,13].

In the present paper, we propose a parallel implicit MPM procedure for the simulation of deformable particles in the context of the finite strain theory as an extension of our previous model based on the infinitesimal strain hypothesis [11,12]. This novel formulation allows for applying a large class of material behaviours like hyperelasticity [14]. Furthermore, a parallel algorithm based on MPI (Message Passing Interface) is proposed in the context of the MPM. It permits to improve considerably the computational performance of our MPM framework. We apply this method to study

* Corresponding author.
E-mail address: saeid.nezamabadi@umontpellier.fr (S. Nezamabadi).

the compaction of a packing of soft particles. The soft-particle packings may undergo volume change as a consequence of particle rearrangements as in hard-particle materials. But, their property of volume change by particle shape and size change under moderate external loads, leads to enhanced space filling. It allows the packing fraction to exceed the random close packing (RCP) limit [15–17]. The compaction and other rheological properties of soft-particle systems beyond this 'jamming' point are still poorly understood. Our results show the capability of the MPM coupled with CD for the investigation of soft particle packings beyond the RCP limit. We focus on the evolution of the packing and effects of particle shape change. As we shall see, the particle material behaviour affects the stress level and its evolution during compaction.

The paper is organised as follows. In Section 2, the new MPM formulation based on the finite strain theory and our contact algorithm are introduced. Section 3 is devoted to the presentation of the implicit MPM resolution. Then, in Section 4 we describe the parallelisation procedure of our MPM-CD method. In Section 5, we focus first on the behaviour of a single particle subjected to axial strain. Then, we analyse the compaction process of a packing of soft circular particles. We conclude with a brief summary and perspectives of this work.

2. Material point method formulation

In this section, we describe the basic formulation of the material point method in the context of finite strain theory. Similar formulations have been presented in our previous papers [11,12] in which the infinitesimal strain theory has been considered, where for modelling soft particles, the MPM has been coupled with the CD method for the treatment of frictional contacts between particles.

Let Ω_t be a domain in $\mathbb{R}^D$, D being the domain dimension, associated with a continuum body, in its actual configuration at time t. Its conservation of mass is described by this continuity equation:

$$\frac{\partial \rho({}^t\mathbf{x}, t)}{\partial t} + \nabla_{{}^t\mathbf{x}} \left(\rho({}^t\mathbf{x}, t) \cdot \mathbf{v}({}^t\mathbf{x}, t) \right) = 0 \quad \text{in } \Omega_t \,, \tag{1}$$

where $\rho({}^t\mathbf{x}, t)$ indicates the material density and $\mathbf{v}({}^t\mathbf{x}, t)$ denotes the velocity field at position ${}^t\mathbf{x}$ (the prefix superscript 't' indicates the time) in the actual configuration Ω_t at time t. The conservation of linear momentum for this continuum body is defined by

$$\nabla_{{}^t\mathbf{x}} \cdot \boldsymbol{\sigma}({}^t\mathbf{x}, t) + \mathbf{b}({}^t\mathbf{x}, t) = \rho({}^t\mathbf{x}, t)\, \mathbf{a}({}^t\mathbf{x}, t) \quad \text{in } \Omega_t \,, \tag{2}$$

where $\boldsymbol{\sigma}({}^t\mathbf{x}, t)$ is the Cauchy stress tensor, $\mathbf{b}({}^t\mathbf{x}, t)$ represents the body force and $\mathbf{a}({}^t\mathbf{x}, t)$ denotes the acceleration at position ${}^t\mathbf{x}$ and time t.

This continuum body is subjected to prescribed displacements and forces on the disjoint complementary parts of the boundary $\partial\Omega_t^u$ (the Dirichlet boundaries) and $\partial\Omega_t^f$ (the Neumann boundaries), both in the actual configuration, respectively. The boundary conditions are then defined by

$$\begin{cases} \mathbf{u}({}^t\mathbf{x}, t) = \hat{\mathbf{u}}(t) & \text{on } \partial\Omega_t^u \,, \\ \boldsymbol{\sigma}({}^t\mathbf{x}, t) \cdot \mathbf{n} = \mathbf{f}(t) & \text{on } \partial\Omega_t^f \,, \end{cases} \tag{3}$$

where $\mathbf{u}({}^t\mathbf{x}, t)$ and $\hat{\mathbf{u}}(t)$ are the displacement field and the prescribed displacement, respectively. Here, $\mathbf{n}$ denotes the outward unit normal vector to $\partial\Omega_t$ and $\mathbf{f}(t)$ is a prescribed load.

In the MPM, the continuum body domain is divided into N_p infinitesimal constant mass elements called material points. Because of this assumption (constant material point mass), the mass conservation relation (1) is self-satisfied. Furthermore, the material points serve as integration points to compute the FEM integrals. The MPM then discretises these integrals through a Dirac delta function by considering a fixed material point mass. Hence, the weak form of the equation of motion (2) in its discretised version can be written as follows by considering the contact interactions between several bodies [11]:

$$\mathbf{M}\, \mathbf{a}_{\text{node}}(t) = \mathbf{f}_{\text{int}}(t) + \mathbf{f}_{\text{ext}}(t) + \mathbf{f}_{\text{c}}(t) \,, \tag{4}$$

where $\mathbf{a}_{\text{node}}$ is the nodal acceleration, $\mathbf{f}_{\text{c}}$ denotes the contact force, which will be illustrated below, and

$$\mathbf{M} = \sum_{p=1}^{N_p} m_p\, \mathbf{N}_p \qquad \text{lumped mass matrix,}$$

$$\mathbf{f}_{\text{int}}(t) = -\sum_{p=1}^{N_p} \mathbf{G}_p\, \boldsymbol{\sigma}_p(t)\, V_p(t) \qquad \text{internal force vector,}$$

$$\mathbf{f}_{\text{ext}}(t) = \sum_{p=1}^{N_p} \mathbf{N}_p\, \mathbf{b}_p(t) + \mathbf{f}_{\text{s}}(t) \qquad \text{sum of body forces and surface tractions } \mathbf{f}_{\text{s}} \,.$$

In the above relations, V_p denotes the material point volume and $\mathbf{N}_p$ is the interpolation matrix or the shape function matrix at a material point p. It relates the quantities associated with the material points (displacement, position$\cdots$) to nodal variables of the element to which the material point belongs. $\mathbf{G}_p$ denotes the gradient of the shape function $\mathbf{N}_p$.

Since there are generally more material points than grid nodes, a weighted squares approach is used to determine nodal velocities $\mathbf{v}_{\text{node}}$ from the material point velocities $\mathbf{v}_p$. Hence, the nodal velocities are obtained by solving the relation

$$\mathbf{P}_{\text{node}}(t) = \mathbf{M}\, \mathbf{v}_{\text{node}}(t) = \textstyle\sum_{p=1}^{N_p} m_p\, \mathbf{N}_p\, \mathbf{v}_p(t) \,, \tag{5}$$

where $\mathbf{P}_{\text{node}}$ is the nodal momentum.

It is also important to note that, as we deal with deformable particle systems, the contact forces $\mathbf{f}_{\text{c}}$ between particles need to be computed using a contact algorithm that accounts for the condition of impenetrability of matter as well as the Coulomb friction law. This contact algorithm combines the MPM and CD methods that was presented in detail in our previous paper [11]. For clarity, in the following, we briefly describe this algorithm.

Let us consider two deformable particles (α and β); see Fig. 1. In the context of the multi-mesh algorithm, a proper background mesh is attributed to each particle. A contact point at the interface between the two particles may be treated by introducing a common background mesh with the same type of grids for the transfer of nodal quantities from the proper meshes to the common mesh. The contact points between the particles α and β are treated at the neighbouring nodes belonging to the common background mesh. Their nodal values involve contributions from the two particles. At a potential contact node i, a normal unit vector $\mathbf{n}_i$, oriented from particle β to particle α, and a tangential unit vector $\mathbf{t}_i$ are defined [18]. As long as the normal velocity v_n ($v_n = (\mathbf{v}_i^{\alpha} - \mathbf{v}_i^{\beta}) \cdot \mathbf{n}_i$)

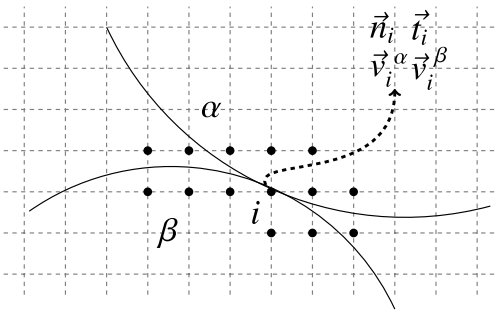

Fig. 1. Geometry of a contact between two soft particles discretised in multi-mesh MPM algorithm. The solid points represent the potential contact nodes; see text.

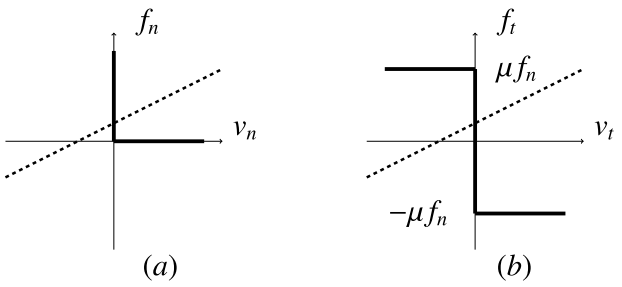

Fig. 2. Contact conditions: (a) Velocity-Signorini complementarity condition as a graph relating the normal relative velocity v_n and normal force f_n; (b) Coulomb friction law as a graph relating the tangential velocity v_t and friction force f_t; μ is the coefficient of friction. The dashed lines represent the linear relations obtained from a linear combination of the equations of dynamics; see text.

remains positive, the normal force f_n is identically zero. But when $v_n = 0$, a non-negative (repulsive) normal force f_n is mobilised at the contact node. These conditions define the velocity-Signorini complementary condition as shown in Fig. 2(a) [19,20]. On the other hand, by combining the equations of motion $\mathbf{P}^{\alpha}_{\text{node}} = \mathbf{M}^{\alpha}\mathbf{v}^{\alpha}_{\text{node}}$ and $\mathbf{P}^{\beta}_{\text{node}} = \mathbf{M}^{\beta}\,\mathbf{v}^{\beta}_{\text{node}}$ at the common node i, we get the following linear relation:

$$f_n = \frac{1}{\Delta t}\,\frac{m_i^{\alpha}\,m_i^{\beta}}{m_i^{\alpha}+m_i^{\beta}}\,v_n + k_n\,, \tag{6}$$

where m_i^{α} and m_i^{β} are the nodal masses of bodies of α and β, respectively, Δt denotes the incremental time, and k_n is an offset force which depends on other contact forces exerted by the neighbouring bodies of α and β. The normal force at all contact nodes are obtained through an iterative process by intersecting the above linear relation with the Signorini graph, as shown in Fig. 2(a).

In a similar vein, the Coulomb law of dry friction is a complementarity relation between the friction force f_t and the tangential velocity v_t ($v_t = (\mathbf{v}_i^{\alpha} - \mathbf{v}_i^{\beta})\cdot\mathbf{t}_i$) at the contact node; see Fig. 2(b). Like the Signorini graph, the Coulomb law is a complementarity relation in the sense that it cannot be reduced to a single-valued function. The equations of motion at the common node i yield

$$f_t = \frac{1}{\Delta t}\,\frac{m_i^{\alpha}\,m_i^{\beta}}{m_i^{\alpha}+m_i^{\beta}}\,v_t + k_t\,, \tag{7}$$

which is intersected with the Coulomb graph to calculate the friction force f_t simultaneously at all contact nodes in the same iterative process used to calculate the normal forces. The convergence to the solution both for contact forces and internal stresses is smooth, and a high precision may be achieved through the convergence criterion.

It is worth noting that in the presented algorithm, a contact may occur between the particles even if they are not physically in contact. Indeed, since the contact is computed on the nodes of the background mesh (not on the material points), the distance between the particles in contact can vary within one element size. The contact force accuracy depends hence on the particle discretisation as well as time discretisation (time step). This issue exists in all contact algorithms and depending on the necessary solution accuracy required for a specified problem, one can adjust the time and/or space resolution. In our case, the proposed contact algorithm allows us to treat rapidly and accurately enough the contact between deformable particles with any arbitrary shape although some local parameters such as contact surface may not be accurately defined.

3. A finite strain formulation for MPM

To complement the continuity equation (1) and the momentum equation (2), we consider a constitutive relationship in the context of the finite strain theory:

$${}^{t}_{0}\mathbf{\Pi}({}^{0}\mathbf{x}, t) = \mathcal{F}^{(r)}({}^{t}_{0}\mathbf{F}({}^{0}\mathbf{x}, t))\,, \tag{8}$$

where ${}^{t}_{0}\mathbf{\Pi}({}^{0}\mathbf{x}, t)$ is the first Piola–Kirchhoff stress tensor at position ${}^{0}\mathbf{x}$ in the initial configuration and at time t. Let ${}^{t}_{0}\mathbf{F}({}^{0}\mathbf{x}, t) = \boldsymbol{\nabla}_{{}^{0}\mathbf{x}}\mathbf{u}({}^{t}\mathbf{x}, t) + \mathbf{I}$ be the deformation gradient tensor, where $\mathbf{I}$ is the second-order identity tensor. Note that ${}^{t}_{0}\mathbf{\Pi}$ and ${}^{t}_{0}\mathbf{F}$ are defined at the actual configuration 't' with respect to the initial configuration at time $t = 0$. ${}^{t}\boldsymbol{\sigma}$ is also related to ${}^{t}_{0}\mathbf{\Pi}$ through

$${}^{t}\boldsymbol{\sigma}({}^{t}\mathbf{x}, t) = \tfrac{1}{{}^{0}J}\,{}^{t}_{0}\mathbf{\Pi}({}^{0}\mathbf{x}, t)\,({}^{t}_{0}\mathbf{F}({}^{0}\mathbf{x}, t))^{T}\,, \tag{9}$$

with ${}^{0}J = \det({}^{t}_{0}\mathbf{F}({}^{0}\mathbf{x}, t))$. Note that, by virtue of the definition of the constitutive relation (8), this framework corresponds to the finite strain theory, and it is not specifically designed for a particular constitutive law. Hence, the material behaviour can cover various nonlinear and complex physical and geometrical evolutions of the continuum body.

4. Finite strain MPM: an implicit-type formalism

In our previous paper [11], a MPM algorithm with an implicit time integration was introduced. In this section, we adopt this approach to our new formulation in the framework of the finite strain theory. Note that the implicit resolution concerns only the nodal parameters whereas those related to the material points are determined explicitly.

Let us advance the solution of (4) from 't' to '$t + \Delta t$' in the context of the implicit resolution. We consider that $\mathbf{f}_{\text{ext}}(t + \Delta t)$ is known, and the grid kinematics is advanced in time as follows:

$$\mathbf{u}_{\text{node}}(t + \Delta t) = \Delta t\;\mathbf{v}_{\text{node}}(t + \Delta t)\,, \tag{10}$$

$$\mathbf{v}_{\text{node}}(t + \Delta t) = \mathbf{v}_{\text{node}}(t) + \Delta t\;\mathbf{a}_{\text{node}}(t + \Delta t)\,. \tag{11}$$

Note that, in Eq. (10), we have $\mathbf{u}_{\text{node}}(t) = 0$ since $\mathbf{u}_{\text{node}}(t + \Delta t)$ is in fact the grid displacement from 't' to '$t + \Delta t$'. From Eqs. (10) and (11), the nodal acceleration at time $t + \Delta t$ is given by

$$\mathbf{a}_{\text{node}}(t + \Delta t) = \frac{1}{\Delta t^2}\,\mathbf{u}_{\text{node}}(t + \Delta t) - \frac{1}{\Delta t}\,\mathbf{v}_{\text{node}}(t)\,. \tag{12}$$

In the context of the finite strain theory, the evaluation of the material point volume V_p changes from t to $t + \Delta t$ according to

$$V_p(t + \Delta t) = {}^{t}J_p\;V_p(t) \tag{13}$$

with ${}^{t}J = \det({}^{t+\Delta t}_{t}\mathbf{F})$.

In an incremental-iterative resolution algorithm, a new estimation of the nodal displacement $\mathbf{u}^{k}_{\text{node}}(t + \Delta t)$ at iteration k is obtained by adding the incremental displacement $\Delta\mathbf{u}^{k}_{\text{node}}$ to the previous estimated displacement:

$$\mathbf{u}^{k}_{\text{node}}(t + \Delta t) = \mathbf{u}^{k-1}_{\text{node}}(t + \Delta t) + \Delta\mathbf{u}^{k}_{\text{node}}\,. \tag{14}$$

To obtain $\Delta\mathbf{u}^{k}_{\text{node}}$ at iteration k, we solve

$$\mathbf{K}^{k-1}\;\Delta\mathbf{u}^{k}_{\text{node}} = \mathbf{R}^{k}\,, \tag{15}$$

where $\mathbf{K}$ is the stiffness matrix and $\mathbf{R}$ refers to the residual term. This equation is the incremental form of relation (4). The terms $\mathbf{K}$ and $\mathbf{R}$ are defined in Appendix A.

This incremental algorithm finds a nodal displacement $\mathbf{u}_{\text{node}}(t+\Delta t)$ that minimises the residual term, $\mathbf{R}$. So, as in [21], we introduce two convergence criteria:

$$C_1 = \frac{\|\Delta\mathbf{u}^{k}_{\text{node}}\|}{\|\Delta\mathbf{u}^{\max}_{\text{node}}\|} < \epsilon_1 \qquad \text{and} \qquad C_2 = \frac{\|\Delta\mathbf{u}^{k}_{\text{node}}\;\mathbf{R}^{k}\|}{\|\Delta\mathbf{u}^{1}_{\text{node}}\;\mathbf{R}^{1}\|} < \epsilon_2\,, \tag{16}$$

where ϵ_1 and ϵ_2 are tolerance parameters on velocities and energy, respectively, $\|\cdot\|$ is the norm operator, $\|\Delta\mathbf{u}^{\max}_{\text{node}}\|$ denotes the maximum value of the norm of the incremental displacement, and $\|\Delta\mathbf{u}^{1}_{\text{node}}\;\mathbf{R}^{1}\|$ indicates the initial value of the inner product of the incremental displacement and residual term.

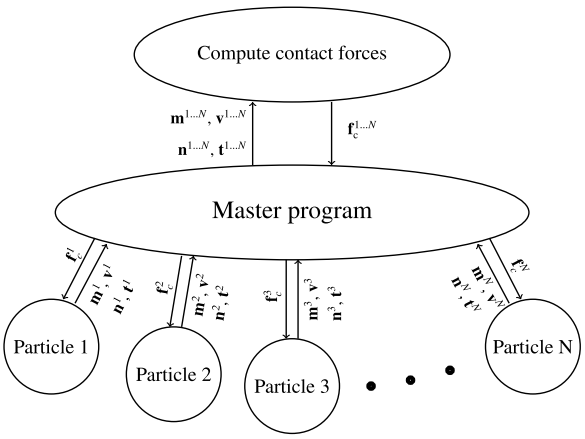

Fig. 3. Scheme of the parallelisation procedure of the MPM-CD framework; N is the number of the particles and, $\mathbf{f}_c$, $\mathbf{m}$, $\mathbf{n}$ and $\mathbf{t}$ represent the contact force, mass, normal and tangential vectors, respectively, for the potential contact nodes of each particle.

5. MPM and parallel computation

The MPM simulations involving a modest number of particles and material points can be performed in a reasonable time on a single-processor workstation. As the number of particles and physical complexity of the numerical model increase, so does the computational resources required. The simulation of 1000 particles, for example, with a sufficient number of material points for their discretisation is not thus suited to a single processor. Hopefully, the required level of computational power can be obtained by parallel MPM simulations. Herein, the goal is to produce a portable parallel implementation that would exhibit good performance scaling up to several hundred processors for large-scale simulations. The code is required to run on parallel computer systems having either shared or distributed memory.

5.1. Parallelisation procedure

The proposed MPM parallel algorithm is of SPMD (Single Program, Multiple Data) style, based on MPI. The particles in the simulation domain are divided into spatial sub-domains. Choosing the number of sub-domains equal to the number of available processors, the data associated with particles in the same sub-domain are stored in the memory of a single processor. The computational effort depends on the resolution of Eq. (4) for each particle, which is closely related to the particle volume. Assuming that the processors have equal performances, to achieve load balance (needed to minimise synchronisation delays), the sub-domains should be chosen such that the sum of volumes of particles is nearly the same in all sub-domains. Hence, the particles in a sub-domain are not necessarily neighbours.

In the proposed MPM algorithm, the resolution of Eq. (4) imposes the computation of the contact forces $\mathbf{f}_c$ for each particle, which depend on the interactions between particles. Since the contact forces are computed on the master process, the only data exchange between the particles (and thus the processors) are the contact forces $\mathbf{f}_c$; see Fig. 3. It is also worth noting that the computation of contact forces on the master process is constant independently of the number of processors and represents less than about 0.5% of the total computational time.

5.2. Load balance

Each MPI thread manages MPM computations of a set of particles, one particle being attributed to only one process. So, the elementary MPM computational weight unit is the weight of a particle. However, particles involved in the global simulation do not exhibit exactly the same volume, and thus the same computational weight. To reach correct performances, the particles have to be distributed in such a way that the weight is well balanced between processes. To do so, we propose the following algorithm for P processes:

1. The N particles are sorted by decreasing radius.
2. The P largest sorted particles are attributed to the P processes.
3. The $P + 1$ particle is attributed to the process with the lightest workload
4. Step 3 is iterated until all particles are attributed.

Fig. 4 displays our load balance algorithm for an example of circular particles in 2D. As the weight here is proportional to the particle surface (in 2D), the total surface of particles $\sum {R_i}^2$ must be well balanced. This approach allows reaching very low load imbalances. For instance, it is less than 1% for $N = 300$ particles (radii of particles ranging from 0.7 mm to 1.2 mm) and $P = 60$ processes.

5.3. Scalability

The scalability of the code was studied with the help of the cluster of the Genotoul Bioinformatics Platform (Toulouse, France). Each compute node embeds 2 Ivy-Bridge 10 cores hyper-threaded microprocessors (2.5 GHz) and the nodes are interconnected through a QDR Infini-Band network for both MPI communications and IO. In our study, the number of processors P varies from 1 to 60, and according to this number at most 20 cores were used per compute node.

As shown in Fig. 5, the scaling is not linear and the efficiency decreases quite fast when P increases. Clearly, such a behaviour can be attributed to the communication bottleneck in rank 0 process. Collective communications involved in data exchange between MPM and Contact Dynamics lead to a large amount of data to be sent or received by rank 0 MPI thread. Such a point should be addressed in future improvements of our code.

6. Numerical examples

The accuracy and efficiency of the proposed algorithm within the finite strain theory are studied through several mechanical compaction tests. In our previous works [11,12], the performance of a similar approach in the framework of the infinitesimal strain hypothesis was shown. We propose two main applications. The first one deals with the uni-axial deformation of a single soft particle. The second example concerns the compaction of a packing of 300 soft particles. To avoid stress gradients in these examples, the gravitational acceleration is set to be zero.

In the MPM, two-dimensional simulations in plane strain conditions were performed. The computation domain was meshed with four-node quadrangular elements. For the applications that we target in the present work, we consider two types of material behaviours [14]: a linear Saint-Venant Kirchhoff constitutive relation

$$\mathbf{S} = \lambda\, \mathrm{Tr}(\boldsymbol{\gamma})\, \mathbf{I} + \mu\, \boldsymbol{\gamma}\,, \tag{17}$$

and a nonlinear Neo-Hookean constitutive law

$$\mathbf{S} = (\lambda\, \ln(J) - \mu)\, \mathbf{C}^{-1} + \mu\, \mathbf{I}\,, \tag{18}$$

where $\mathbf{S}$ is the second Piola–Kirchhoff stress tensor and related to $\boldsymbol{\Pi}$ through $\boldsymbol{\Pi} = \mathbf{F}\,\mathbf{S}$. Let $\mathbf{C} = \mathbf{F}^T\mathbf{F}$ be the right symmetric Cauchy–Green tensor. $\boldsymbol{\gamma}$ denotes the Green–Lagrange strain tensor ($\boldsymbol{\gamma} = \frac{1}{2}(\mathbf{C} - \mathbf{I})$) and $J = \det(\mathbf{F})$. λ and μ represent the Lamé coefficients.

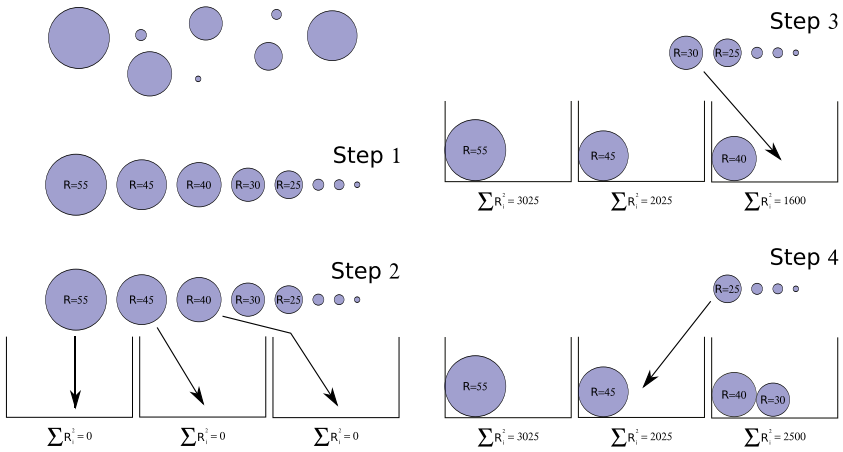

Fig. 4. Load balance algorithm. A set of circular particles (in 2D) is shown, R_i^2 being written in each particle, and distributed in 3 processes. The total workload $\sum R_i^2$ is updated at each step.

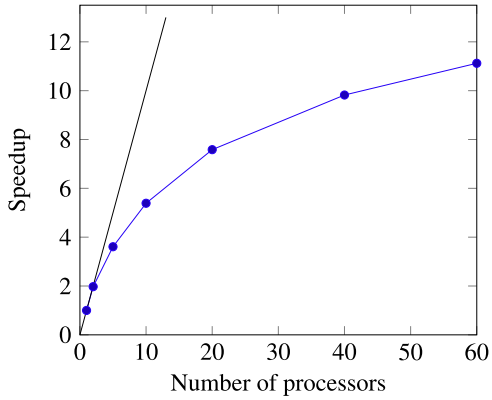

Fig. 5. Measured speedup for the MPM-CD simulation of 300 particles. The line represents perfect scaling.

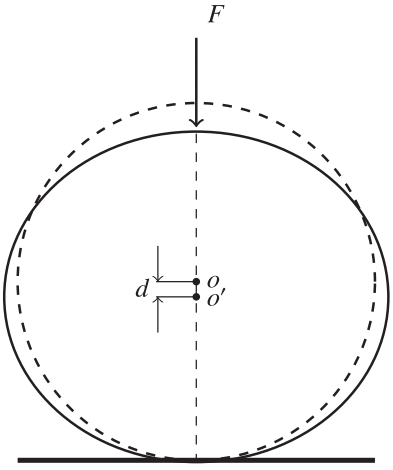

Fig. 6. Contact geometry between a single particle and a rigid plate.

6.1. Axial compaction of a single particle

We consider here the case of a single cylindrical particle subjected to axial compression. The particle has a diameter of $D = 20$ mm and is compressed between two rigid walls as shown in Fig. 6. The bottom wall is fixed and the top wall moves downwards at a constant velocity of 0.5 m/s. The time step is set to $\Delta t = 0.1$ μs. To compare the infinitesimal and finite strain formulations in the context of the MPM, the linear Hookean and Saint-Venant Kirchhoff elastic behaviours (see Eq. (17)) are considered. In the two cases, the Lamé coefficients and density of the particles were set to $\lambda = 100$ MPa, $\mu = 1.5$ MPa and $\rho = 990$ kg/m^3, respectively. Fig. 7 presents the normal contact force F as a function of displacement d of the centre of the particle. In the two cases, a quasi-linear evolution of force with displacement is observed but with a small deviation for $\frac{d}{D} > 0.05$ towards a lower level of force. This behaviour corresponds to the prediction of the Hertz analysis for a cylinder of unit length [22]:

$$F = \frac{\pi}{4} E^* d \,, \tag{19}$$

where E^* is the effective elastic modulus defined as $E^* = E/(1-\nu^2)$ with E being Young's modulus and ν Poisson's ratio. Furthermore, the predicted values of forces by the infinitesimal and finite strain formulations are not very different. This means that, as a result of the small value of the time step, the second order terms in the Green–Lagrange strain rate have little effect on the total strain.

We carried out the same test by considering a Neo-Hookean particle (see Eq. (18)). We set $\mu = 1.5$ MPa, $\rho = 990$ kg/m^3, and three values of $\lambda = 0$, 3 and 100 MPa. These different values of λ define the compressibility of the particle, i.e. for $\lambda = 0$ the particle is fully compressible whereas for $\lambda = 100$ MPa the particle

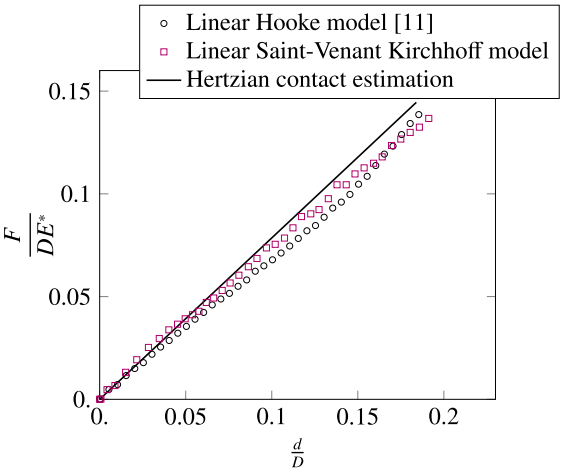

Fig. 7. Normal contact force applied on a single particle as a function of the displacement of the particle centre for two different behaviours.

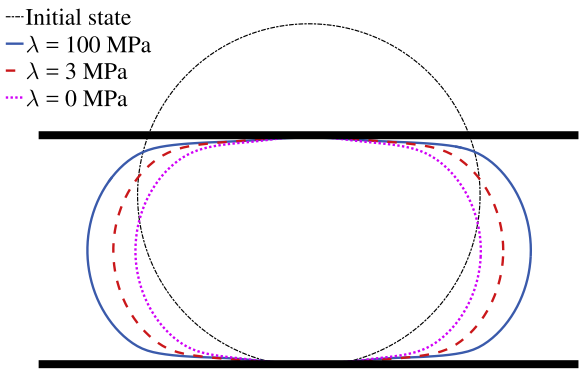

Fig. 8. Geometry of a single Neo-Hookean particle and it's deformed configurations at vertical strain $\gamma_{yy} = 20\%$ for different values of λ. Although the deformed particles seem to touch the two walls only over a short segment at the centre, the material points belonging to the boundary elements between the particle and the bottom and top walls are actually within the contact zone. The observed gap is due to the background mesh element thickness.

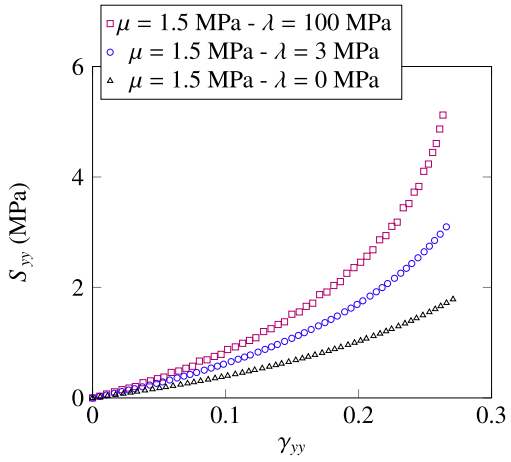

Fig. 9. The stress–strain diagrams for a single Neo-Hookean particle subjected to diametrical compression for several values of λ.

is quasi-incompressible. The deformed particles at vertical strain $\gamma_{yy} = 20\%$ for these values of λ are shown in Fig. 8.

We also note the decrease of the lateral extension as the particle compressibility increases. This extension is negligible for the fully compressible particle (λ = 0 MPa) (see Fig. 8). It can be explained by the fact that for the incompressible particle, the volume of the compressed portion can migrate to the non-contact portion more efficiently as a result of its dense structure [23]. Fig. 9 displays the second Piola–Kirchhoff stress S_{yy} as a function of the Green–Lagrange strain γ_{yy}. We see that the stress increases as λ increases. In other words, deforming less compressible particles requires a larger force.

6.2. Compaction of a packing of elastic particles

In this section, we investigate the compaction of a packing of elastic particles using the Neo-Hookean material behaviour. By means of MPM simulations, we study the evolution of different packing properties (packing fraction, connectivity etc.). We consider a packing of 300 particles confined inside a rectangular box. The initial configuration is prepared by means of DEM simulations. A uniform distribution of the particle diameters by volume fractions in the range [2, 4] mm is introduced. This polydispersity allows avoiding long-range ordering. We simulate the compaction process by moving the top wall downwards at constant velocity

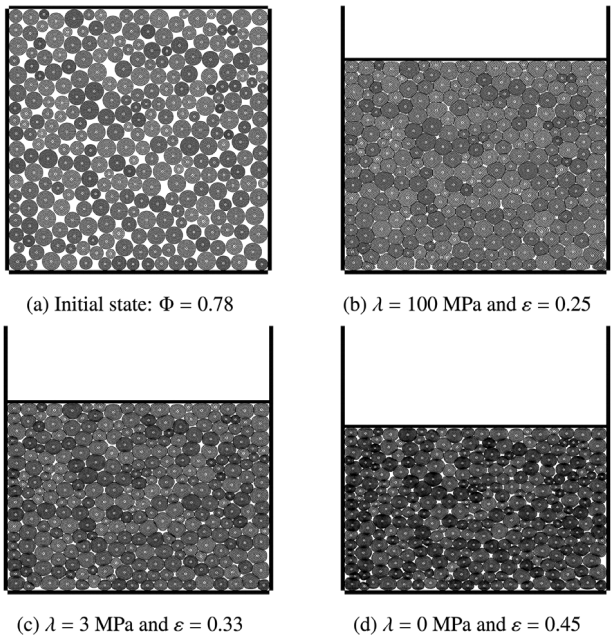

Fig. 10. A snapshot of the initial configuration (a) and three snapshots of the compaction of a packing of soft particles with Neo-Hookean behaviour for packing fraction of 0.97 and several values of the λ (b–d). Note that, despite the same value of the packing fraction, the packing volumes are different due to the different compressibilities of the particles. The black points represent the material points.

of 2 m/s and with a time step of $\Delta t = 0.1$ μs. We consider the Neo-Hookean particles with the same material parameters as in the previous section. The gravitational acceleration is set to be zero in order to avoid stress gradients. There is no friction between the particles, and between the particles and the walls.

Fig. 10 represents the snapshots of the compaction test for different values of λ . The packing fraction $\Phi = V_S/V$, where V_S is the volume of particles and V the total volume, increases by particle shape change and at the end of the compaction nearly the whole space is filled by the particles. The shapes of the particles gradually change from circular to nearly polygonal as shown in Fig. 10. Note that the gaps observed between particles are related to the meshing resolution, which may be increased for a finer discretisation of the contact zone. Moreover, as mentioned before, since the less compressible particles can elongate more, the pores between these particles are more rapidly filled even for a low global deformation.

The above feature is more clearly highlighted in Fig. 11. It shows the cumulative volume deformation of the particles defined by $\ln(V_S/V_{S_i})$, where V_{S_i} is the initial volume of the particles, and the cumulative vertical strain ε as a function of the packing fraction Φ. The latter is expected to vary due to the elastic volume change of the particles as a result of elastic compressibility of the particles as well as the variation of the total volume V due to particle rearrangements and shape change. Since the width of the box is constant, we have

$$\ln\left(\frac{V_S}{V_{S_i}}\right) = \ln\left(\frac{\Phi}{\Phi_i}\right) + \varepsilon \tag{20}$$

with $\varepsilon = \ln(h/h_i)$, where h_i is the initial height of the sample. In Fig. 11, the data for three values of λ coincide up to $\Phi \simeq 0.8$. Beyond this packing fraction, ε and $\ln(V_S/V_{S_i})$ vary at different nearly linear rates for each λ value. As expected, this rate increases as λ (or compressibility) decreases. Note that for λ = 100 MPa (quasi-incompressible particles), the volume variation of particles is negligibly small as shown in Fig. 11. Moreover, one can consider

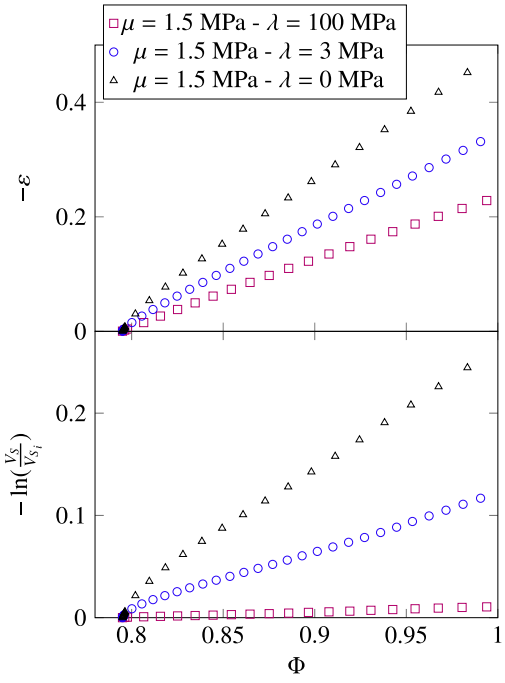

Fig. 11. Evolution of the cumulative vertical strain ε and, the total particles volume change $\ln(V_S/V_{S_i})$ as a function of the packing fraction Φ for several values of λ.

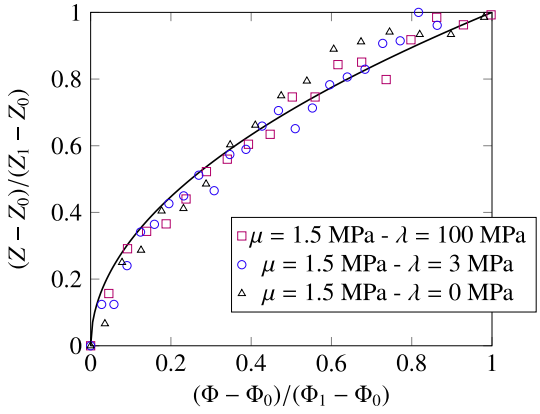

Fig. 12. Evolution of the excess mean coordination number $Z - Z_0$ as a function of excess packing fraction $\Phi - \Phi_0$ for several values of λ. The solid line is power-law fit $(\Phi - \Phi_0)^{0.5}$; see Eq. (21).

$\Phi \simeq 0.8$ as the jamming point above which no particle rearrangements occur anymore, and thus the packing evolution is only due to particle shape change.

The mean coordination number Z is an important parameter, which evolves with the evolution of the packings. Fig. 12 displays Z as a function of Φ. We see that by normalising the excess coordination number $Z-Z_0$, where Z_0 is the mean coordination number at the jamming point, by Z_1-Z_0, where Z_1 is the coordination number at $\Phi_1 \simeq 1$, and $\Phi - \Phi_0$ by $\Phi_1 - \Phi_0$, all data points collapse on a single plot that is well fitted by a power-law function:

$$\frac{Z-Z_0}{Z_1-Z_0} = \left(\frac{\Phi-\Phi_0}{\Phi_1-\Phi_0}\right)^{0.5} . \tag{21}$$

A similar power-law behaviour was observed by several authors specially in the case of emulsions and foams [17,24,25] in the following form:

$$Z - Z_0 = z_0(\Phi - \Phi_0)^{\beta} . \tag{22}$$

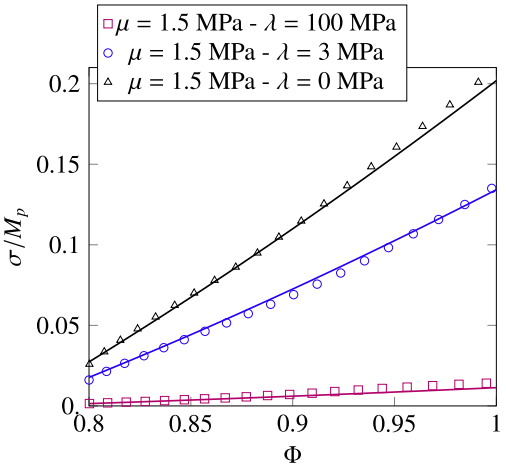

Fig. 13. The normalised applied stress as a function of packing fraction normalised by the particle P-wave modulus M_p for several values of λ. The lines represent the predicted behaviour by the model of compaction introduced in this paper; see Eq. (23).

These two last equations coincide by setting $\beta = 0.5$ and $z_0 = (Z_1 - Z_0)/(\Phi_1 - \Phi_0)^{0.5}$. As in our study, for all cases, we have $Z_0 \simeq 4$ for Φ_0 and $Z_1 \simeq 5.6$ for Φ_1, one gets $z_0 \simeq 3.6$. This value is fully consistent with O'Haren et al. (2003) [24] who predicted that z_0 is equal to 3.5 ± 0.3 and $\beta \simeq 0.5 \pm 0.03$ in 2D. It is also interesting to note that the material behaviour of the particles has almost no effect on these results (see Fig. 12), in agreement with the references [17,24,25], which observed that the evolution of the coordination number with packing fraction is independent of space dimension, interaction potential and polydispersity.

The evolution of the applied stress σ beyond the jamming point allows for a macroscopic analysis of the packing evolution. Fig. 13 shows σ, computed from the contact forces acting on the bottom wall and normalised by the particle P-wave modulus M_p ($M_p = \lambda + 2\mu$) as a function of Φ. We note a nonlinear behaviour for three cases with different rates. As in the case of one particle simulations, we observe also that the required force to compress the packing increases with the particle compressibility. These observations may be explained by the fact that beyond the jamming point the packing behaves almost like a continuum medium as there are no more particle rearrangements. This assumption leads to a logarithmic relation between σ and Φ (see Appendix B):

$$\frac{\sigma}{M_p} = -\frac{Z\Phi}{Z+\frac{M_p}{c_1 K_p}}(\ln(\Phi) + c_2) , \tag{23}$$

where K_p is the particle bulk modulus ($K_p = \lambda + \mu$ in 2D), c_1 is a parameter depending on the particle material behaviour and c_2 is a constant term. The coordination number Z is also defined as a function of Φ by Eq. (21). The predictions of this model (23) are in good agreement with our MPM simulations shown in Fig. 13 with $c_2 \simeq 0.27$, and $c_1 \simeq 0.01$ for $\lambda = 100$ MPa, $c_1 \simeq 0.23$ for $\lambda = 3$ MPa and $c_1 \simeq 1.3$ for $\lambda = 0$ MPa. Note that, although this model seems to predict well the applied stress σ as a function of Φ, at high packing fractions, the Neo-Hookean particles can only overfill the remained little pores for much higher stresses (involving smaller and smaller radii of curvature) but when the packing fraction tends to 1, the corresponding applied stress should tend to infinity. Hence, this model does not hold at high values of the packing fraction. In our simulations, to resolve correctly the small radii of curvature at the contact zones between particles, one should refine in the same proportion the discretisation.

In order to analyse the particle deformations and volume change during the compaction of the packings, we also consider the evolution of the distribution of the equivalent von Mises strain γ_{eq} and

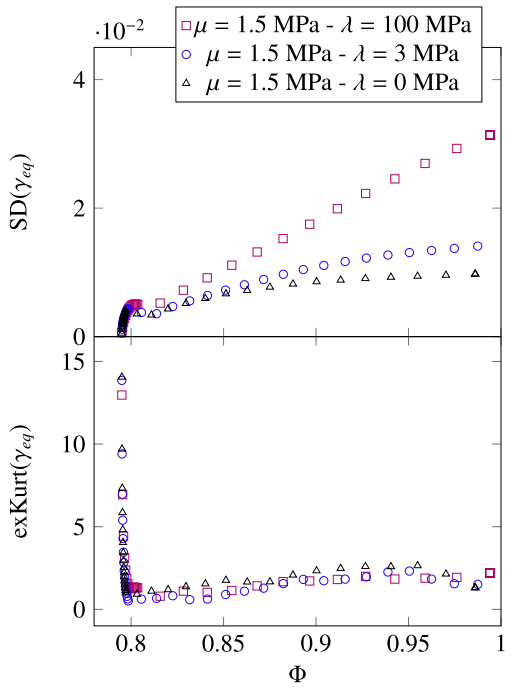

Fig. 14. Evolution of the standard deviation *SD* and excess Kurtosis *exKurt* of the equivalent von Mises strain, γ_{eq} as a function of the packing fraction Φ for several values of λ.

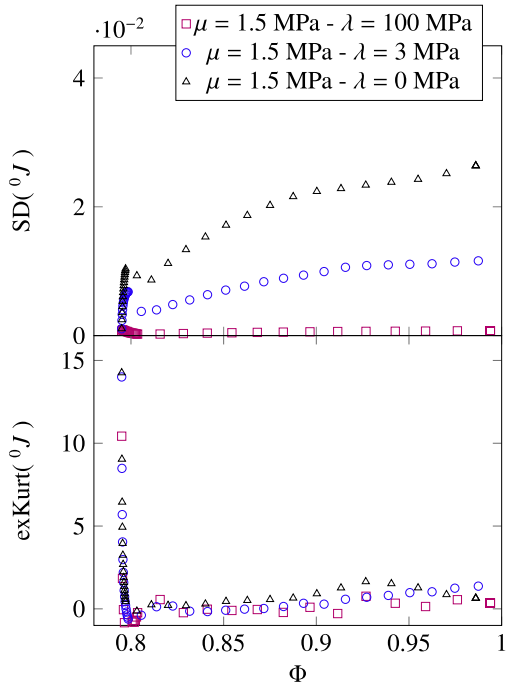

Fig. 15. Evolution of the standard deviation *SD* and the excess Kurtosis *exKurt* of ^0J as a function of the packing fraction Φ for several values of λ.

the Jacobian of deformation gradient ^0J (see Eq. (9)), respectively. Here, γ_{eq} is defined as

$$\gamma_{eq} = \sqrt{\tfrac{2}{3}\,\boldsymbol{\gamma}^d : \boldsymbol{\gamma}^d}\,, \tag{24}$$

with $\boldsymbol{\gamma}^d = \boldsymbol{\gamma} - \frac{1}{3}\,\mathrm{Trace}(\boldsymbol{\gamma})\,\mathbf{I}$. To characterise the shapes of these distributions, we consider here their standard deviation and excess kurtosis. Fig. 14 displays the standard deviation and excess kurtosis of γ_{eq} as a function of Φ. The standard deviation of γ_{eq} for the three values of λ coincide up to $\Phi \simeq 0.8$, but beyond this value they vary at different rates. In the quasi-incompressible case ($\lambda = 100$ MPa), the standard deviation is larger than in compressible cases. This trend can be explained by the occurrence of more important stress chains between particles when their compressibility decreases. The values of the excess kurtosis of γ_{eq} distributions for several values of λ coincide, and they tend to a positive value about 2 beyond the jamming point. This value is compatible with a Leptokurtic distribution, which shows heavier tails than the normal distribution.

Finally, the standard deviation and the excess kurtosis of the Jacobian of deformation gradient ^0J as a function of Φ are shown in Fig. 15. As expected, the standard deviation for $\lambda = 100$ MPa (quasi-incompressible particles) is almost zero since there is no particle volume change. The standard deviation is larger for the fully compressible particles ($\lambda = 0$ MPa). It is due to the larger possible deformation of the particles in this case. However, the kurtosis is nearly zero, meaning that the ^0J distributions are nearly normal.

7. Conclusion

In this paper, we improved our approach for modelling soft-particle systems developed in [11]. In this novel approach, the finite strain formulation is used in the context of the implicit Material Point Method (MPM). The MPM allows one to take into account the realistic mechanical behaviour of individual particles. Coupling the MPM with the Contact Dynamics (CD) method makes it possible to deal correctly with frictional contacts between particles.

It was shown that two MPM formulations (infinitesimal and finite strain) are similar. The finite-strain formulations can host more complex constitutive behaviours such as hyperelasticity for the particles. Furthermore, to improve computational performance, a parallelisation procedure was proposed in the framework of this algorithm. Although the efficiency of this procedure declines with increasing number of processors, it is still useful for decreasing the computational cost.

The uni-axial compaction of a packing of soft particles was simulated using MPM by considering several values of particle compressibility (from quasi-incompressible to fully compressible particles). The packing with more compressible particles can undergo larger deformations under the action of lower compressive stress due to considerable particle volume changes and occurrence of weaker stress chains between particles. It was shown that this stress beyond the jamming state varies logarithmically with packing fraction. This behaviour was explained by introducing a simple model. Another interesting result of this work concerns the evolution of the coordination number, which can be related to the packing fraction by a power-law function beyond jamming transition.

Acknowledgements

This work/project (ID 1502-607) was publicly funded through ANR (the French National Research Agency) under the "Investissements d'avenir" programme with the reference ANR-10-LABX-001-01 Labex Agro and coordinated by Agropolis Fondation, France under the frame of I-SITE MUSE (ANR-16-IDEX-0006). We are also grateful to the genotoul bioinformatics platform Toulouse Midi-Pyrenees (Bioinfo Genotoul) for providing computing resources.

Conflict of interest

Saeid Nezamabadi, Xavier Frank, Jean-Yves Delenne, Julien Averseng and Farhang Radjai state that there are no conflicts of interest.

Appendix A. Definitions of K and R

The implicit integration in the context of MPM takes into account the discretised equation of the motion:

$$\mathbf{M}\,\mathbf{a}_{\text{node}}(t+\Delta t) = \mathbf{f}_{\text{int}}(t+\Delta t) + \mathbf{f}_{\text{ext}}(t+\Delta t)\,, \tag{A.1}$$

By considering that the external force at time $t+\Delta t$ is known, $\mathbf{f}_{\text{ext}}(t+\Delta t)$, and by assuming an incremental-iterative Newton solution strategy, the linearised equation of motion at iteration k is

$$\mathbf{K}^{k-1}\,\Delta\mathbf{u}^{k}_{\text{node}} = \mathbf{R}^{k}\,, \tag{A.2}$$

where

$$\mathbf{K}^{k-1} = \frac{1}{\Delta t^2}\,\mathbf{M} - \sum_{p=1}^{N_p} V_p(t)\,\mathbf{G}_p\;{}^{t+\Delta t}_{t}\mathbb{H}^{k-1}_{p}\;\mathbf{G}_p \tag{A.3}$$

$$\mathbf{R}^{k} = \mathbf{f}_{\text{ext}}(t+\Delta t) + \mathbf{f}^{k-1}_{\text{int}}(t+\Delta t) - \mathbf{M}\,\mathbf{a}^{k-1}_{\text{node}}(t+\Delta t)\,, \tag{A.4}$$

with

${}^{t}J_p\;{}^{t+\Delta t}\boldsymbol{\sigma}_p = {}^{t+\Delta t}_{t}\mathbb{H}_p\;{}^{t+\Delta t}_{t}\mathbf{F}_p$.

Note that in the last relation, ${}^{t+\Delta t}\mathbb{H}_p$ can be obtained using Eq. (9) and the constitutive relation (8).

Appendix B. Relation between the applied stress, σ, and the packing fraction, Φ, for a packing under uniaxial compression

We assume that the packing of particles behaves almost as a continuum medium beyond the jamming point under uniaxial compression. Hence, in this range the applied stress σ may be related to the cumulative vertical strain ε through an effective P-wave modulus M:

$$\sigma = M\varepsilon\,. \tag{B.1}$$

Here, the particle and pore volume changes can be assumed to be the same, implying that the effective P-wave modulus is proportional to the packing fraction: $M = \Phi M_p$ with M_p the particle P-wave modulus. One may further assume that the particle bulk modulus K_p relates the volume increment $\mathrm{d}V_S$ of particles to the effective stress increment $\mathrm{d}\sigma_S$ in particles:

$$K_p\,\frac{\mathrm{d}V_S}{V_S} = -\mathrm{d}\sigma_S\,. \tag{B.2}$$

σ can be related to σ_S as follows:

$$\sigma = c_1 Z \Phi \sigma_S\,, \tag{B.3}$$

where c_1 is a material constant to determine. Given that $\mathrm{d}\varepsilon = \mathrm{d}V_S/V_S - \mathrm{d}\Phi/\Phi$ and using Eqs. (B.1), (B.2) and (B.3), the following differential equation to solve is obtained:

$$(Z + \tfrac{M_p}{c_1 K_p})\mathrm{d}\sigma = \left[(Z + \tfrac{M_p}{c_1 K_p})\tfrac{\sigma}{\Phi} - M_p Z\right]\mathrm{d}\Phi + \tfrac{M_p}{c_1 K_p}\tfrac{\sigma}{Z}\mathrm{d}Z\,, \tag{B.4}$$

By knowing that there is a relationship between Z and Φ (see Eq. (21)), the integration of the differential equation (B.4) is given:

$$\tfrac{\sigma}{M_p} = -\tfrac{Z\Phi}{Z+\frac{M_p}{c_1 K_p}}(\ln(\Phi) + c_2)\,, \tag{B.5}$$

where c_2 is the integral constant.

References

[1] P.A. Cundall, O.D.L. Strack, Géotechnique 29 (1979) 47–65.
[2] H. Matuttis, S. Luding, H. Herrmann, Powder Technol. 109 (2000) 278–292.
[3] J. Moreau, Eur. J. Mech. A Solids 13 (1994) 93–114.
[4] M. Jean, F. Jourdan, B. Tathi, Proceeding of The International Deep Drawing Research Group (IDDRG 1994), in: Handbooks on Theory and Engineering Applications of Computational Methods, 1994.
[5] F. Radjai, V. Richefeu, Mech. Mater. 41 (2009) 715–728.
[6] F. Da Cruz, F. Chevoir, D. Bonn, P. Coussot, Phys. Rev. E 66 (2002) 051305.
[7] M. Cloitre, R. Borrega, F. Monti, L. L., Phys. Rev. Lett. 90 (2003) 068303.
[8] R. Bonnecaze, M. Cloitre, Adv. Polym. Sci. 236 (2010) 117–161.
[9] A. Favier de Coulomb, M. Bouzid, P. Claudin, E. Clément, B. Andreotti, Phys. Rev. Fluids 2 (2017) 102301.
[10] M. Barnabe, N. Blanc, T. Chabin, J.-Y. Delenne, A. Duri, X. Frank, V. Hugouvieux, E. Lutton, F. Mabille, S. Nezamabadi, et al., Innovative Food Sci. Emerg. Technol. (2017).
[11] S. Nezamabadi, F. Radjai, J. Averseng, J.-Y. Delenne, J. Mech. Phys. Solids 83 (2015) 72–87.
[12] S. Nezamabadi, T. Nguyen, J.-Y. Delenne, F. Radjai, Granular Matter 19 (2017) 8.
[13] V. Acary, B. Brogliato, Numerical Methods for Nonsmooth Dynamics. Applications in Mechanics and Electronics, Springer, 2009.
[14] S. Nezamabadi, H. Zahrouni, J. Yvonnet, Comput. Mech. 47 (2011) 77–92.
[15] J.G. Berryman, Phys. Rev. A 27 (1986) 1053.
[16] S. Torquato, T.M. Truskett, P.G. Debenedetti, Phys. Rev. Lett. 84 (2000) 2064.
[17] M. van Hecke, J. Phys.: Condens. Matter 22 (2010) 033101.
[18] P. Huang, X. Zhang, S. Ma, X. Huang, Internat. J. Numer. Methods Engrg. 85 (2011) 498–517.
[19] M. Jean, in: A. Salvadurai, J. Boulon (Eds.), Mechanics of Geomaterial Interfaces, Elsevier Science Publisher, Amsterdam, 1995, pp. 463–486.
[20] B. Brogliato, Nonsmooth Mechanics, Springer, London, 1999.
[21] J. Guilkey, J. Weiss, Internat. J. Numer. Methods Engrg. 57 (2003) 1323–1338.
[22] K. Johnson, Contact Mechanics, Cambridge University Press, Cambridge, 1999.
[23] Y.-L. Lin, D.-M. Wang, W.-M. Lu, Y.-S. Lin, K.-L. Tung, Chem. Eng. Sci. 63 (2008) 195–203.
[24] C. O'Hern, L. Silbert, A. Liu, S. Nagel, Phys. Rev. E 68 (2003) 011306.
[25] J. Zhang, T.S. Majmudar, M. Sperl, R. Behringer, Soft Matter 6 (2010) 2982–2991.